



Identification and characterization of second-generation EZH2 inhibitors with extended residence times and improved biological activity

Received for publication, October 15, 2020, and in revised form, January 21, 2021. Published, Papers in Press, January 30, 2021.

<https://doi.org/10.1016/j.jbc.2021.100349>

Jacob I. Stuckey, Nico R. Cantone, Alexandre Côté, Shilpi Arora, Valerie Vivat, Ashwin Ramakrishnan, Jennifer A. Mertz, Avinash Khanna, Jehrod Brenneman, Victor S. Gehling, Ludivine Moine, Robert J. Sims III, James E. Audia , Patrick Trojer, Julian R. Levell, and Richard T. Cummings* 

From the Constellation Pharmaceuticals, Cambridge, Massachusetts, USA

Edited by John Denu

The histone methyltransferase EZH2 has been the target of numerous small-molecule inhibitor discovery efforts over the last 10+ years. Emerging clinical data have provided early evidence for single agent activity with acceptable safety profiles for first-generation inhibitors. We have developed kinetic methodologies for studying EZH2-inhibitor-binding kinetics that have allowed us to identify a unique structural modification that results in significant increases in the drug-target residence times of all EZH2 inhibitor scaffolds we have studied. The unexpected residence time enhancement bestowed by this modification has enabled us to create a series of second-generation EZH2 inhibitors with sub-pM binding affinities. We provide both biophysical evidence validating this sub-pM potency and biological evidence demonstrating the utility and relevance of such high-affinity interactions with EZH2.

A diverse array of histone posttranslational modifications contribute to the dynamic regulation of chromatin architecture. Discrete combinations of these modifications have been proposed to form a putative “histone code” that can be read out by effector proteins and complexes, to regulate transcription by controlling access to individual genomic loci (1–3). Aberrant alterations in histone coding mechanisms have been extensively linked to the altered transcriptomes observed in tumors (4). Further, genetic alterations in chromatin regulatory proteins are among the most frequent mutational events observed across numerous cancer types (5). Accordingly, there

is significant therapeutic interest in pharmacological modulation of key chromatin regulatory proteins (6, 7).

The multisubunit Polycomb Repressive Complex 2 (PRC2) is a key chromatin regulator that exhibits histone methyltransferase activity on H3 lysine 27 (H3K27). The catalytic core of PRC2 consists of an SAM-dependent histone methyltransferase (either EZH1 or EZH2), an H3K27me3-binding subunit (EED), and a Zn-finger, scaffolding subunit (SUZ12). Multiple heterozygous point mutations have been observed in the EZH2 subunit of PRC2. These mutations are a recurrent genomic feature observed in multiple cancer types, with the highest frequency presenting in non-Hodgkin’s lymphoma (8). Biochemically, these mutations alter the catalytic activity of EZH2, thereby resulting in aberrant, EZH2-mediated global increases in H3K27me3 levels (9–11). Furthermore, EZH2 catalytic function has been implicated more broadly in oncology with EZH2-mediated gene silencing contributing not only to oncogenic pathway activation but also to acquired drug resistance and suppression of antitumor immune responses in T cells (8, 12). Accordingly, EZH2 catalytic inhibition is being explored clinically as a therapeutic approach in multiple solid tumor and hematological malignancies with Tazemetostat recently being the first approved EZH2 targeting drug for use in epithelioid sarcoma (7, 13–15).

Clinical agents that target EZH2 exert their effect through one of two mechanisms of inhibition. The first inhibitors described belong to multiple series of pyridone-containing small molecules (EZH2i) that target a pocket located near the interface of EZH2 and EED. The critical nature of the pyridone moiety was made clear after multiple reports emerged detailing cocrystal structures of several of these inhibitors with PRC2. These analyses revealed that the sole point of overlap between the compound-binding pocket on EZH2 and the SAM-binding site was the area occupied by the pyridone of the respective compounds. This structural insight not only illuminated the previously unknown physical basis for the compounds’ SAM-competitive mechanism of inhibition but also cemented the central role of the pyridone in the context of these EZH2 inhibitors (16–18). Some of the more recent PRC2 inhibitor reports have focused on the biochemical role of H3K27me3 binding to the EED subunit of PRC2. The

This article contains [supporting information](#).

* For correspondence: Richard T. Cummings, richard.cummings@constellationpharma.com.

Present address for Jacob I. Stuckey, Jennifer A. Mertz, Robert J. Sims III, and James E. Audia: Third Rock Ventures, Boston, MA, USA.

Present address for Alexandre Côté: Schrodinger, New York, NY, USA.

Present address for Shilpi Arora: Exo Therapeutics, Cambridge, MA, USA.

Present address for Ashwin Ramakrishnan: Bristol-Myers Squibb, Cambridge, MA, USA.

Present address for Avinash Khanna: Hansoh Bio, Rockville, MD, USA.

Present address for Jehrod Brenneman: Bridge Biotherapeutics, Inc, Cambridge, MA, USA.

Present address for Ludivine Moine: Blueprint Medicines, Cambridge, MA, USA.

Kinetic characterization of potent EZH2 inhibitors

H3K27me3-EED binding event in the context of PRC2 is well characterized as an allosteric stimulator of EZH2 methyltransferase activity (19, 20). Accordingly, small molecules that potently antagonize the EED–H3K27me3 interaction also allosterically inhibit EZH2 catalytic function. The clinical utility of EED-targeted small molecules is yet to be determined, but preclinically, these molecules have resulted in tumor growth inhibition similar to that observed for SAM-competitive PRC2 inhibitors (15, 21, 22). Meanwhile, multiple SAM-competitive EZH2 inhibitors have demonstrated clinical activity in the absence of dose-limiting toxicities (13). Observation of emerging clinical profiles, in addition to pre-clinical studies in murine models, has led us to hypothesize that unlocking the full therapeutic potential of EZH2 inhibitors will require molecules that achieve more comprehensive, durable target engagement than can be achieved with existing clinical EZH2 inhibitors.

Recent mechanistic studies into one subseries of SAM-competitive EZH2 inhibitors have demonstrated that these molecules exhibit slow, tight-binding behavior. Detailed kinetics studies led to estimated binding affinities of <100 pM for allosterically activated PRC2 for the most potent compound characterized (23). Characterization of such high-affinity interactions to elucidate structure–activity relationships (SARs) is challenging using traditional, equilibrium-based assay formats. Theoretical treatment of binding equilibria by Motulsky and Mahan in 1983 first noted that the required equilibration time for an interaction with ligand concentrations equal to its K_d under pseudo-first-order conditions, is a function of the drug-target residence time (τ) (24–27). This can result in interactions that will require multiple days of equilibration to accurately assess affinity if the protein-inhibitor complex exhibits sufficiently slow k_{off} values. This concept was recently highlighted in a report detailing biosensor-based kinetic methodologies to quantify single-digit pM affinities in order to circumvent the practical limitations of equilibrium-based biochemical assays (28). Unfortunately, biosensor-based methodologies, such as surface plasmon resonance (SPR), have limited utility in studying PRC2-inhibitor kinetics because of the large complex size, long residence time of EZH2 inhibitors, and the practical limitations of assessing kinetics in the activated state because of nonspecific interactions between cationic histone peptides and the gold biosensor surface.

We recently reported residence time enhancement for EZH2 inhibitors as assessed by a jump dilution method utilizing TR-FRET technology (29). Herein, we describe the full scope of biochemical approaches we used to kinetically characterize high-affinity, pyridone-containing EZH2 inhibitors (EZH2i). Key technical nuances not detailed previously are described here that enabled kinetic characterization of second-generation EZH2i. Further, in this work, we also expand the methodology for k_{on} determination to enable fully quantitative potency assessments. Finally, we expand on the structure–kinetic relationships (SKRs) described previously (29) by showing the universality of the key structural motif to significantly enhance EZH2-inhibitor residence time across all scaffolds tested. The

insights from our kinetic studies have enabled us to drive our second-generation series SAM-competitive EZH2 inhibitors to sub-pM biochemical potencies that correlate with enhanced tumor cell killing *in vitro* and *in vivo*.

Results

Enzymatic jump dilution assays

The standard biochemical assay for assessing enzyme-inhibitor residence times is a jump dilution-based methodology in which enzyme and inhibitor are pre-equilibrated at an inhibitor concentration equal to its IC_{90} value as determined in an equilibrium-based biochemical assay (30). The pre-equilibration is followed by a rapid, 100-fold dilution that results in an inhibitor concentration equal to its IC_{10} value. However, the observed sub-nM EZH2i potencies coupled with the relatively slow turnover of H3 by EZH2 ($k_{cat} \sim 25/h$) make dilution to IC_{10} simply impractical. Further, this cannot be compensated for by increasing the concentration of cofactor competitor due to the radioactive assay readout, because radioactive SAM is stored in a sulfuric acid solution, which precludes its use at concentrations $> \sim 5 \times K_m$ without substantially altering buffer pH.

To overcome these challenges, we applied a modified jump dilution methodology in which inhibitors were diluted to their Cheng–Prusoff (31) adjusted IC_{50}^{app} at the highest possible SAM concentration. A mathematical correction was then applied to k_{obs} to account for rebinding during the establishment of equilibria, thus allowing a more accurate residence time estimate (Supplementary Note 1). To corroborate our estimated residence time values, we compared them to SPR-determined values using a specialized methodology for analysis of long residence time compounds with a test set of EZH2i including clinical stage compounds and compounds 1–3, (Fig. 1). Overall, we observed good agreement with the estimated compound residence time for basal PRC2 (complex in the absence of H3K27me3 activator peptide) between the two methodologies in spite of the differing pH (8.5 *versus* 7.4) and salt concentrations (0 *versus* 150 mM NaCl) of the biochemical and SPR buffers, respectively. The most significant outlier in this set can be accounted for because the residence time of GSK126 under these conditions is simply too short to reliably quantitate enzymatically in our assay setup. Ultimately, this modified jump dilution methodology quickly became inadequate for our purposes as a result of continued increases in EZH2i residence times. This could not be circumvented by simply running longer reaction times due to the limited stability of SAM in aqueous buffers, and was further limited by our inability to accurately estimate compound IC_{50} values.

Development of TR-FRET-binding assay to measure inhibitor kinetics

In order to circumvent the limitations of using EZH2 catalytic readouts to estimate inhibitor residence times, we developed a time-resolved fluorescence energy transfer (TR-FRET) assay to directly measure free EZH2 as a function of time using a biotinylated EZH2 inhibitor that was designed

Kinetic characterization of potent EZH2 inhibitors

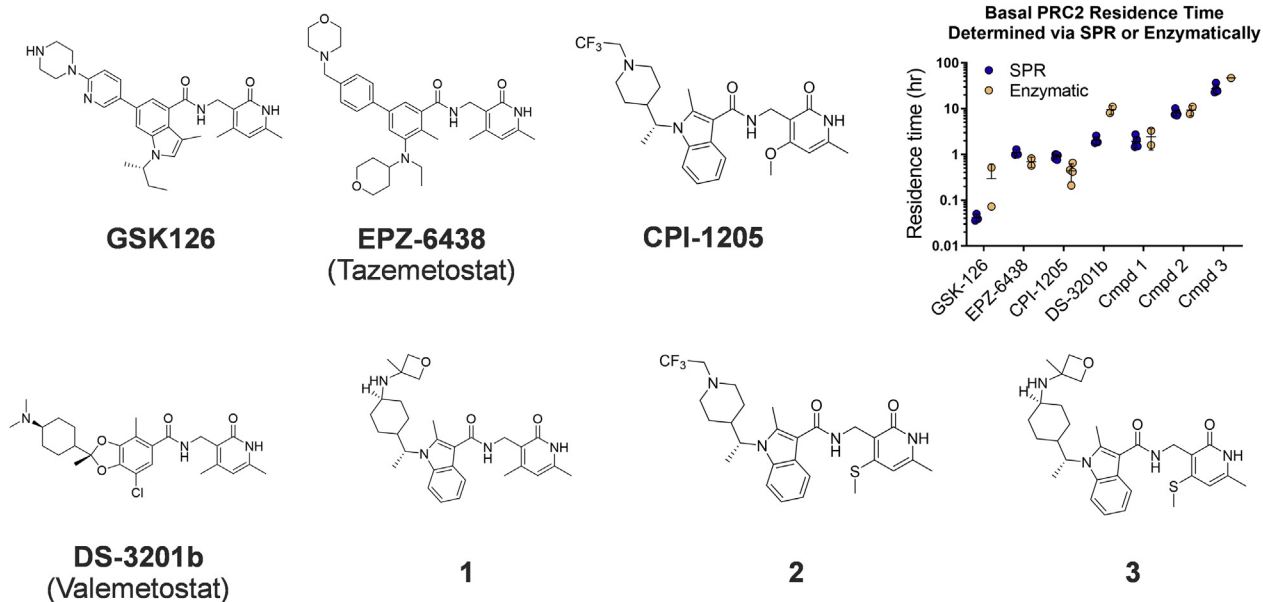


Figure 1. Comparison of SPR-determined residence times and residence times determined using modified jump dilution methodology. Close agreement between the two methodologies was observed for all compounds in this set with GSK126 presenting the most significant divergence as a result of a comparatively short residence time under these conditions. Data are individual replicates with error bars representing the standard deviation of the mean.

based upon literature precedent (biotin-EZH2i, 4, Fig. 2A) (32). The interaction between biotin-EZH2i and His-tagged PRC2 is detected using streptavidin allophycocyanin (SA-APC) and an Eu- α His antibody (Fig. 2B). While the final, measured TR-FRET complex is identical to other standard TR-FRET-based binding assays, assay execution with this system is particularly nuanced. This nuance stems from the altered affinity and

kinetics of the biotin probe when complexed with SA-APC. In order to avoid the altered equilibration time observed with the SA-APC:Biotin-EZH2i complex and PRC2, we explored the impact of order of addition on detection of free PRC2. In doing so, we identified conditions that result in effectively instantaneous equilibration between biotin-EZH2i and pre-equilibrated Eu- α His:PRC2 complex. The SA-APC is then

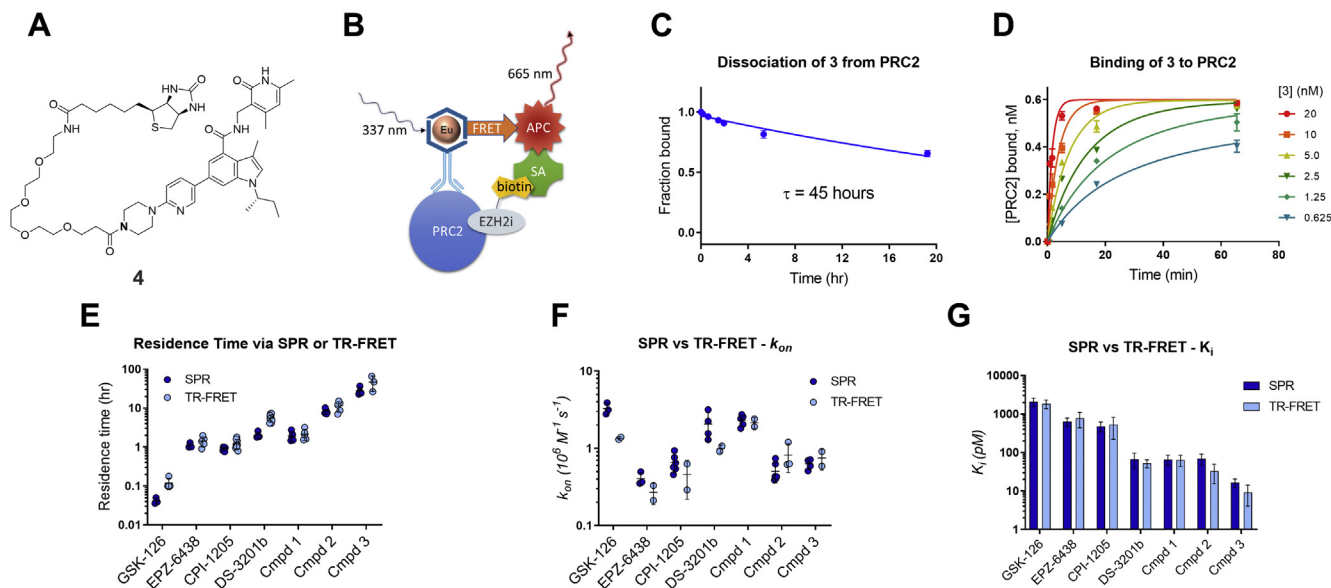


Figure 2. Characterization of EZH2i using a TR-FRET-binding assay. All data are in the context of basal PRC2. *A*, biotin-EZH2i used in TR-FRET methodology. *B*, Depiction of final complex observed using TR-FRET readout. *C*, example PRC2-EZH2i dissociation curve measured using TR-FRET-based methodology. Data are plotted as the average of two technical replicates with error bars representing the standard deviation of the mean. *D*, example PRC2-EZH2i association curves measured using TR-FRET-based methodology. Data are plotted as the average of two technical replicates with error bars representing the standard deviation of the mean. *E*, comparison of residence time values obtained in SPR and TR-FRET assay formats. Data are individual replicates with error bars representing the standard deviation of the mean. *F*, comparison of association rate constant values obtained in SPR and TR-FRET assay formats. Data are individual replicates with error bars representing the standard deviation of the mean. *G*, comparison of calculated inhibitor dissociation constant values obtained from kinetic parameters in either SPR or TR-FRET assay formats from the data displayed in *E* and *F* ($K_i = \frac{k_{off}}{k_{on}}$) where error bars represent propagated error.

Kinetic characterization of potent EZH2 inhibitors

added at a concentration for which its saturation of the biotin-probe bound to EZH2 is also effectively instantaneous (Fig. S1, A and B). Under these conditions, we were able to quantitatively measure free PRC2 across a concentration range of 1.4–1000 pM with excellent linearity with respect to free PRC2 *versus* TR-FRET ratio. The signal and, accordingly, its linearity with respect to [PRC2], peaked between 5 and 10 min following SA-APC addition. Both signal and linearity were stable until ~20 min post SA-APC addition. Peak linearity was achieved at 11 min following SA-APC addition ($R^2 > 0.99$), thus providing an adequate window of time for reagent addition followed by signal readout (Fig. S2, A and B).

We utilized this platform for detection of free EZH2 in two different schematics (Schemes SI and SII, respectively): (1) a jump dilution-based format to monitor dissociation of a pre-bound inhibitor over time to determine k_{off} values and (2) a format to monitor compound association with EZH2 over time to determine k_{on} values. For schematic 1, [PRC2] bound to inhibitor or inhibitor-bound fraction can be plotted *versus* time and fit to a single-phase exponential decay to determine k_{off} (Fig. 2, C). Importantly, this can be run under dialysis conditions to ensure compound rebinding does not result in an overestimation of the drug-target residence time. Rebinding was found to be significant for EZH2i where $\tau > 100$ h and for those compounds, only data under dialysis conditions is reported. Data treatment for schematic 2 requires additional nuance for accurate characterization (*vide infra*).

EZH2i-binding mechanism determination

An example compound titration using schematic 2 is shown in Figure 2D. We tested multiple compounds across multiple scaffolds with a range of k_{off} values (determined using jump dilution procedure outlined in schematic 1). For each of the compounds tested, we observed a clear linear relationship in a plot of k_{obs} *versus* [I] (Fig. S3). This relationship is indicative of a single-step binding mechanism (25, 26), in contrast not only to the previously proposed two-step binding mechanism of slow-tight binding EZH2i, but also to many other characterized long residence time compounds for other protein targets (23, 25). Further, the observed linear relationship of k_{obs} *versus* [I] was not affected by allosteric activation of PRC2 using H3K27me3 activator peptide (Fig. S3, C and D). Finally, we corroborated this observation using both enzymatic methodologies and from the SPR data generated (Fig. S4).

The final consideration for data treatment in these experiments stems from the fact that the concentrations of inhibitor used for our association experiments approach that of the total concentration of PRC2 in the sample, requiring treatments based on second-order reaction conditions. Thus, to obtain estimates of the k_{on} values for the compounds tested, binding curves were fit to the integrated rate equation for a reversible, bimolecular association reaction. The solution to this has been presented numerous times in various forms, with the form used here shown in Supplementary Note II (<https://www.researchgate.net/post/Any-literature-reference-for-the-kinetics-of-reversible-bimolecular-association/581b9f813d7f4be7e503a435/citation/download>) (33–35).

We next compared the agreement of the kinetic parameters using our TR-FRET-based methodologies to the values obtained for the test set of compounds evaluated previously by SPR. All kinetic parameters were in excellent agreement between the two methodologies (Fig. 2, E and F), consequently producing similar estimates for compound-binding affinities (K_i , Fig. 2, G). Taken together, these results indicate that our TR-FRET-based methodology is suitable for accurately determining compound-PRC2 kinetic parameters and, therefore, binding affinity.

Allosteric modulation of compound potency

Intriguingly, the aforementioned allosteric stimulation of EZH2 from H3K27me3 activator peptide has also been shown to modulate the residence time of EZH2 inhibitors (23), a phenomenon we also observed with compound 5 during the course of our mechanistic studies (Fig. S3, C and D). Utilizing our TR-FRET binding assay, we sought to explore this phenomenon across a panel of EZH2 inhibitors. We found that the residence time of every inhibitor increased, although the extent of increase was highly variable (Fig. 3, A). To date, we have not observed a clear SKR that can explain the selectivity for activated relative to basal PRC2, but we suspect it is related to the fact that pyridone-based EZH2i also interacts with the EED subunit as a result of their binding at an interface between EZH2-EED (16–18).

Intrigued by the observed allosteric modulation of EZH2i residence time, we probed for residence time modulation of CPI-1205 by an EED small-molecule antagonist, MAK683. In contrast to experiments with activator peptide (Fig. 3, A), we did not observe an increase in the residence time of CPI-1205 by MAK683 (Fig. 3, B). Nonetheless, the presence of an EEDi negated residence time enhancement by addition of activator peptide (Fig. 3, C). Interestingly, these data directly indicate that EED-targeted small molecules and pyridone-containing EZH2 inhibitors can co-occupy the same PRC2 complex, providing the molecular basis for a simultaneous, orthogonal, PRC2-targeting approach. Notably, as expected from our MOI studies, there was no effect of allosteric stimulation of EZH2 on compound association kinetics (Fig. 3, D).

In order to potentially gain insight into the biologically relevant PRC2 state, we compared cellular potencies of a panel of EZH2i with their residence time values obtained in the basal or activated state of PRC2. While we found a general correlation with both values, it was stronger with the H3K27me3 mark reduction EC_{50} values in HeLa cells for the compound residence times in the activated state, particularly for the most potent compounds in the panel, suggesting that activated PRC2 is the more biologically relevant state (Fig. 3, E and F). Therefore, our subsequent kinetic studies described here were conducted in the context of activated PRC2.

Residence time enhancement imparted by 4-thiomethyl pyridone

We recently reported that, quite unexpectedly, the residence time of compound 2, the 4-thiomethyl analog of CPI-1205,

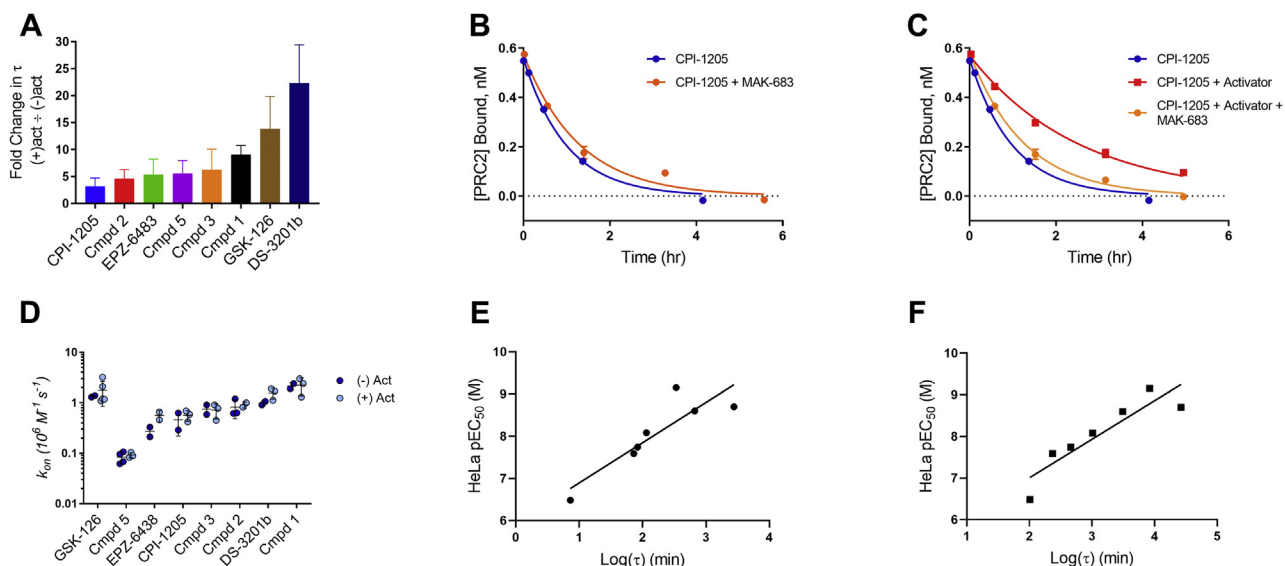


Figure 3. Exploration of allosteric modulation of EZH2i potencies. *A*, effect of allosteric modulation on inhibitor residence times for EZH2 inhibitors used to develop kinetic methodologies. Error bars represent propagated error from measured values used in calculation. *B*, modulation of CPI-1205 residence time by MAK683 (EEDi). Representative data are plotted as the average of two technical replicates (\pm) standard deviation. The residence time of CPI-1205 for basal PRC2 is 1.2 ± 0.3 h (mean \pm SD of nine biological replicates each in duplicate). For basal PRC2 in the presence of $10 \mu\text{M}$ MAK683, the residence time of CPI-1205 is 0.97 ± 0.1 h (average \pm SD of three biological replicates each in duplicate). *C*, MAK683 ($10 \mu\text{M}$) inhibition of CPI-1205 residence time enhancement by H3K27me3 activator peptide ($10 \mu\text{M}$). Representative data are plotted as the average of two technical replicates \pm standard deviation. The residence time of CPI-1205 PRC2 in the presence of H3K27me3 activator peptide and MAK-683 (10 mM each) is 1.3 ± 0.2 h (mean \pm SD of four biological replicates each in duplicate). *D*, comparison of association rate constant values of EZH2i (\pm) $10 \mu\text{M}$ H3K27me3 activator peptide. Data are individual replicates with error bars representing the standard deviation of the mean. *E* and *F*, plots of residence time values for basal (*E*; R^2 0.78) and activated (*F*; R^2 0.82) PRC2 versus $p\text{EC}_{50}$ values for H3K27me3 mark reduction in HeLa cells.

(Fig. 4, A), displayed an order of magnitude increase in inhibitor residence time (29) (Fig. 4, B). Applying our methodology described here for k_{on} determination, we observed that

the residence time enhancement observed for compound 2 was not accompanied by any sort of compensation in k_{on} relative to CPI-1205 (Fig. 3, D); therefore, the extended

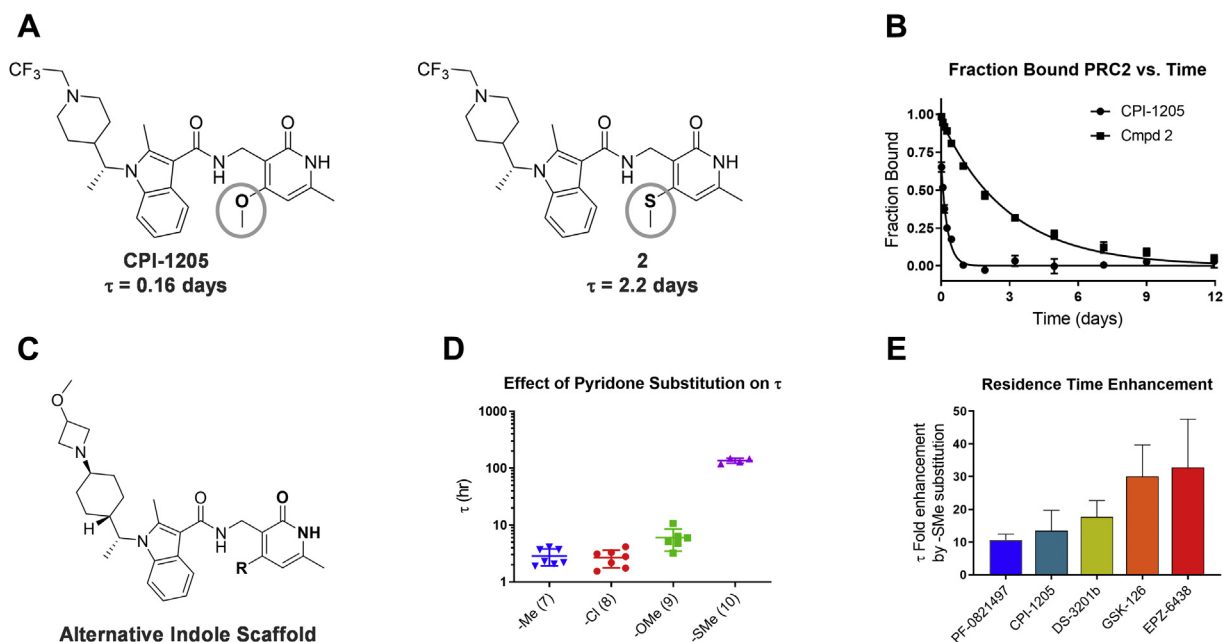


Figure 4. Universal enhancement of EZH2i residence time by 4-thiomethyl pyridone substitution. *A* and *B*, residence time comparison of CPI-1205 with its matched pair, 4-thiomethyl analog 2. Data in *B* are representative data with each point being the average of duplicates and error bars the standard deviation of the mean. *C* and *D*, structure of alternative indole scaffold explored during inhibitor development efforts and residence time values for various functional group substitutions at the 4-position of the pyridone moiety, respectively. For *D* data are individual replicates with error bars representing the standard deviation of the mean. *E*, 4-thiomethyl pyridone substitution leads to residence time enhancements for clinical-stage EZH2i. Error bars represent propagated error from measured values used in calculation.

Kinetic characterization of potent EZH2 inhibitors

residence time resulted in an improvement in the overall binding affinity (Fig. 4, B). This striking observation, coupled with the critical nature of the pyridone moiety for conferring SAM-competitive inhibition of EZH2, drove us to further explore this observation. We performed a focused SKR study in which the substituent at the 4-position of the pyridone was systematically varied between -Me, -Cl, -OMe, and -SMe in the context of an alternative, indole-based scaffold related to CPI-1205/compound 2 (Fig. 4, C). Strikingly, only the -SMe substituent was able to dramatically extend inhibitor residence times on EZH2 (Fig. 4, D).

Having observed this -SMe effect on two distinct indole-containing scaffolds, we next sought to interrogate the universality of the residence time enhancement by generating 4-thiomethyl analogs of 4 clinical stage EZH2i, in addition to CPI-1205 (Fig. S5). We found that residence time was dramatically enhanced in the context of each scaffold. The most strongly impacted scaffolds were EPZ-6438 (Tazemetostat) and GSK126 with both scaffolds exhibiting a ~30-fold residence time enhancement when employing a 4-thiomethyl substitution (Fig. 4, E).

Mechanistic and biophysical validation of EZH2i with femtomolar binding affinity

We plotted the individual kinetic parameters of the compounds profiled (Figs. 1–4) versus the respective pK_i (M) values calculated from those parameters. The kinetically determined K_i values spanned several orders of magnitude and were driven almost exclusively through residence time increases (Fig. 5, A and B). Strikingly, the most potent K_i

estimated in this set was sub-pM (13; $\frac{k_{off}}{k_{on}} = 130$ fM (pK_i (M) = 12.88), Figure 5, A–C). Closer examination of the 4-thiomethyl-containing compound 13 indicates that the compound possesses a residence time on activated PRC2 on the order of several months (Fig. 5, B–D; $\tau = 2300$ h = ~3.0 months). We confirmed the stability of recombinant pentameric PRC2 in the TR-FRET assay conditions by assessing its catalytic activity over time when stored at 25 °C in assay buffer. We found that the complex was very stable in the assay conditions with no loss in catalytic activity observed after 10 days, indicating a half-life for complex stability of months (Fig. S6).

We also confirmed that the MOI for compound 13 was maintained (SAM-competitive) relative to previous pyridone-containing EZH2i by examining the effect of SAM on its EZH2 association kinetics. Addition of SAM to these experiments resulted in a dose-dependent reduction in k_{on}^{app} . Importantly, we observed excellent agreement with the K_m of SAM (400 nM) for PRC2 and the EC_{50} for SAM-mediated reductions in k_{on}^{app} for 13 (740 nM; Fig. S7). We also performed mass spectral analysis of compound 13 following ~2-day incubation with supra-stoichiometric amounts of PRC2 and found that the compound was recovered unmodified, indicating that the extreme residence time of the compound is not achieved through enzymatic processing of the compound (Fig. S8).

We next sought biophysical corroboration of the extreme potency observed through characterization of compound-binding kinetics. We chose to utilize ligand-induced protein thermal stabilization methodologies because of its

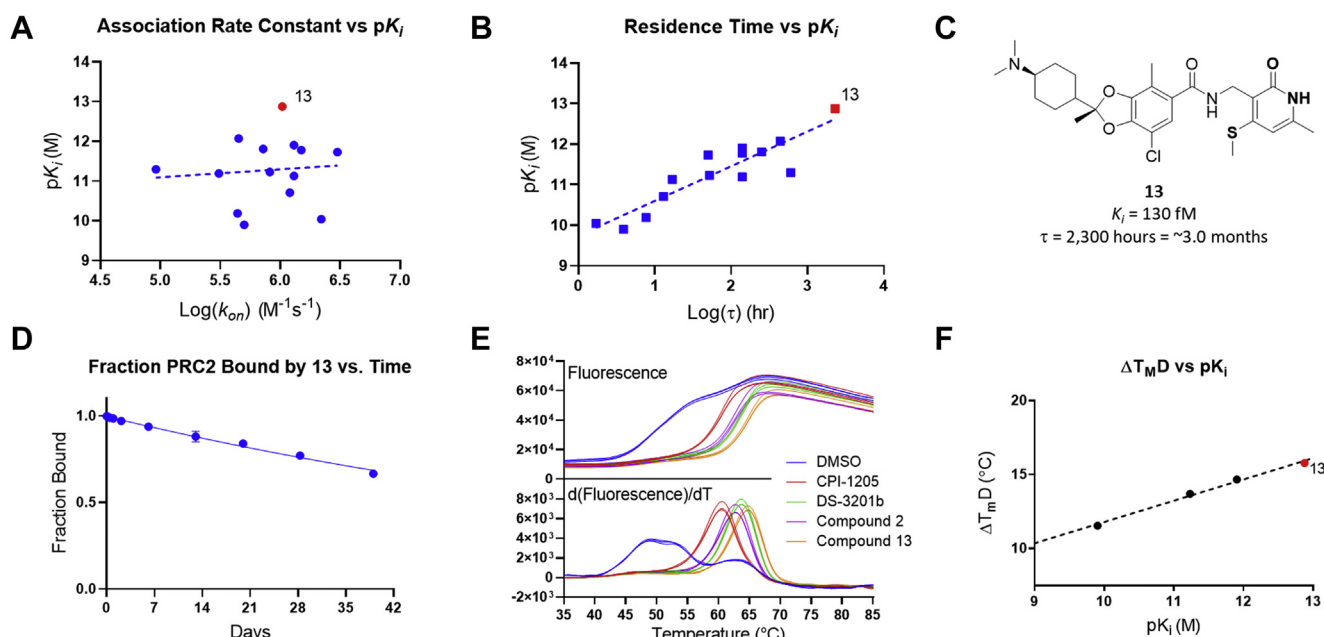


Figure 5. Characterization of high-affinity EZH2i. A and B, contribution of individual kinetic parameters to compound-binding affinities. C, structure of sub-pM, S-methyl-containing EZH2i, 13. D, representative dissociation curve for 13. Data are plotted as the average of two technical replicates with error bars being the standard deviation of the mean: $\tau = 2300 \pm 300$ h (mean \pm SD, five biological replicates each performed in duplicate). E, thermal melt curve plots of selected EZH2 inhibitors (N = 3 for each sample). ΔT_{mD} (mean \pm SEM [°C]): CPI-1205 (11.54 \pm 0.05); 2 (13.69 \pm 0.00); DS-3201b (14.66 \pm 0.00); 13 (15.78 \pm 0.00). F, correlation of ΔT_{mD} with kinetically determined pK_i for EZH2i.

demonstrated utility in estimating the potency of the biotin–streptavidin interaction ($K_d \sim 1$ fM) (36). We selected four compounds, including 13, estimated to have K_i values spanning nearly three orders of magnitude. We tested the thermal stabilization of pentameric PRC2 by these compounds using differential scanning fluorimetry. Under the conditions tested, thermally induced unfolding of PRC2 exhibits multiphasic behavior as evidenced by the first derivative of the fluorescence melting curve (Fig. 5, E). Interestingly, incubation of PRC2 with each of the compounds in our test set resulted in not only a dramatic stabilization of the first melting peak ($\Delta T_{m,D} = 11.54\text{--}15.78$ °C), but also condensed the melting curve to a single transition (Fig. 5, E, lower panel). Further, we found that 13 exhibited significantly greater stabilization of PRC2 relative to the other compounds. This observation holds in terms of both overall melting curve stabilization ($\Delta T_{m,B}$ of 9.2 °C; Fig. 5, E, upper panel) and the first melting peak in the derivative of the dimethylsulfoxide (DMSO) control melting curves ($\Delta T_{m,D} = 15.78$ °C; Fig. 5, E, lower panel). These data biophysically demonstrate that 13 does, in fact, have a significantly higher affinity interaction with PRC2 than the other compounds tested. Notably, the $\Delta T_{m,D}$ value for these compounds did not correlate with pIC_{50} values obtained from a 24-h enzymatic assay using very dilute PRC2 (15 pM), highlighting the impractical equilibration time required for accurate assessments of such high-affinity interactions (Fig. S9). Crucially, however, we found that the $\Delta T_{m,D}$ values of these were correlated with pK_i values obtained from our kinetic experiments, providing strong biophysical evidence of our kinetically determined affinity estimates (Fig. 5, F). Additionally, we found a similar change in T_m and potency rank when assayed in the biochemical assay buffer (Fig. S10) again suggesting that the affinities determined in different buffers were maintained.

Intrigued by the apparent noncovalent nature of inhibition, we sought to further improve the affinity of 13 by constraining the amide linker between the dioxolane heterocycle and the 4-thiomethyl pharmacophore in order to generate CPI-1328 (Fig. 6, A). This rigidification resulted in an improved potency of CPI-1328 relative to 13 (Fig. 6, A and B). We observed that the potency increases are driven primarily through increases in the residence time of the molecule and not through

any significant changes in the measured association rate constant (Fig. 6, B). The even longer residence time of CPI-1328 prompted us to check residual catalytic activity at the final assessed time points in the jump dilution experiment. Importantly, we found that % catalytic activity was in good agreement with the measured amount of liberated PRC2 (Fig. S11), indicating that PRC2 is recovered unmodified following compound dissociation.

These results strongly argue for a wholly noncovalent interaction between these inhibitors and PRC2. If reversible covalent bond formation was responsible for the femtomolar affinity bestowed by the 4-thiomethyl pyridone, conformational constraint of the 4-thiomethyl pyridone would have been expected to drive affinity increases by properly positioning the functional group for covalent bond formation. Kinetically, this would manifest improved potency *via* the association phase of the interaction, which was not observed (Fig. 6). Importantly, the ring cyclization constraint we introduced would not be expected to impact the electronics of the pyridone, which could affect the apparent affinity through impacting both the reactivity of the functionality and the stability of a covalently bound species. Therefore, we conclude that the femtomolar binding affinities we have observed for these compounds are achieved through strictly noncovalent interactions.

Cellular and in vivo impact of enhanced compound potencies

The extreme affinity observed in our *in vitro* biochemical experiments led us to inquire whether there are any biological implications of these measurements. We first compared compound residence times to the cellular potencies of our compounds in an H3K27me3 mark reduction assay in HeLa cells. While we found a general correlation with cellular EC_{50} values, the relationship between residence time and EC_{50} in this assay appears to asymptotically approach a limit for the EC_{50} value at $\sim 0.5\text{--}1$ nM (Fig. 7, A), suggesting this to be the lower limit of this cellular assay and may reflect the total concentration of PRC2 found in HeLa cells, with the most potent compounds effectively titrating the available enzyme. Regardless, this plateau suggests that there is a limit on the extent that residence time and compound affinity can drive cellular potency in this assay. Importantly, however, we also examined the impact of residence time on cell killing in

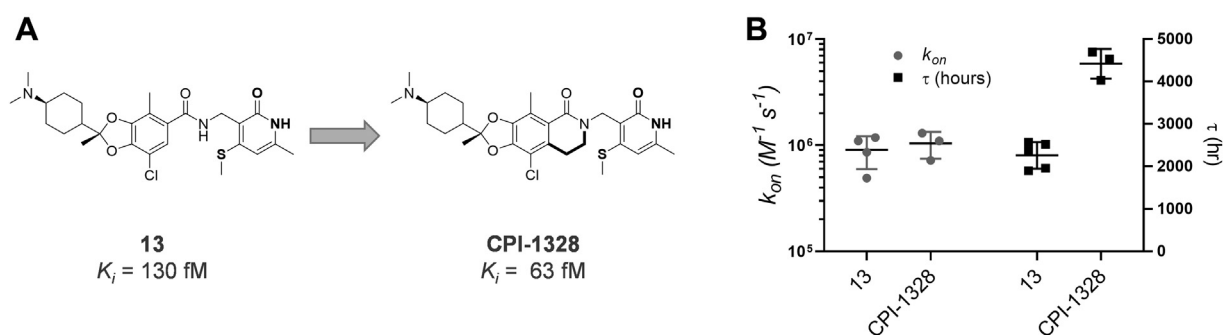


Figure 6. Residence time enhancement driven through rational design. A, conformational restriction of 13 to produce CPI-1328. K_i values were calculated from kinetic parameters displayed in B. B, comparison of kinetic parameters for 13 and CPI-1328. Error bars represent the standard deviation of the measurements. For 13: $k_{on} = 9.1 (\pm 3) \times 10^5$ $M^{-1} s^{-1}$; $\tau = 2300 \pm 300$ h. For CPI-1328: $k_{on} = 1.0 (\pm 0.2) \times 10^6$ $M^{-1} s^{-1}$; $\tau = 4400 \pm 200$.

Kinetic characterization of potent EZH2 inhibitors

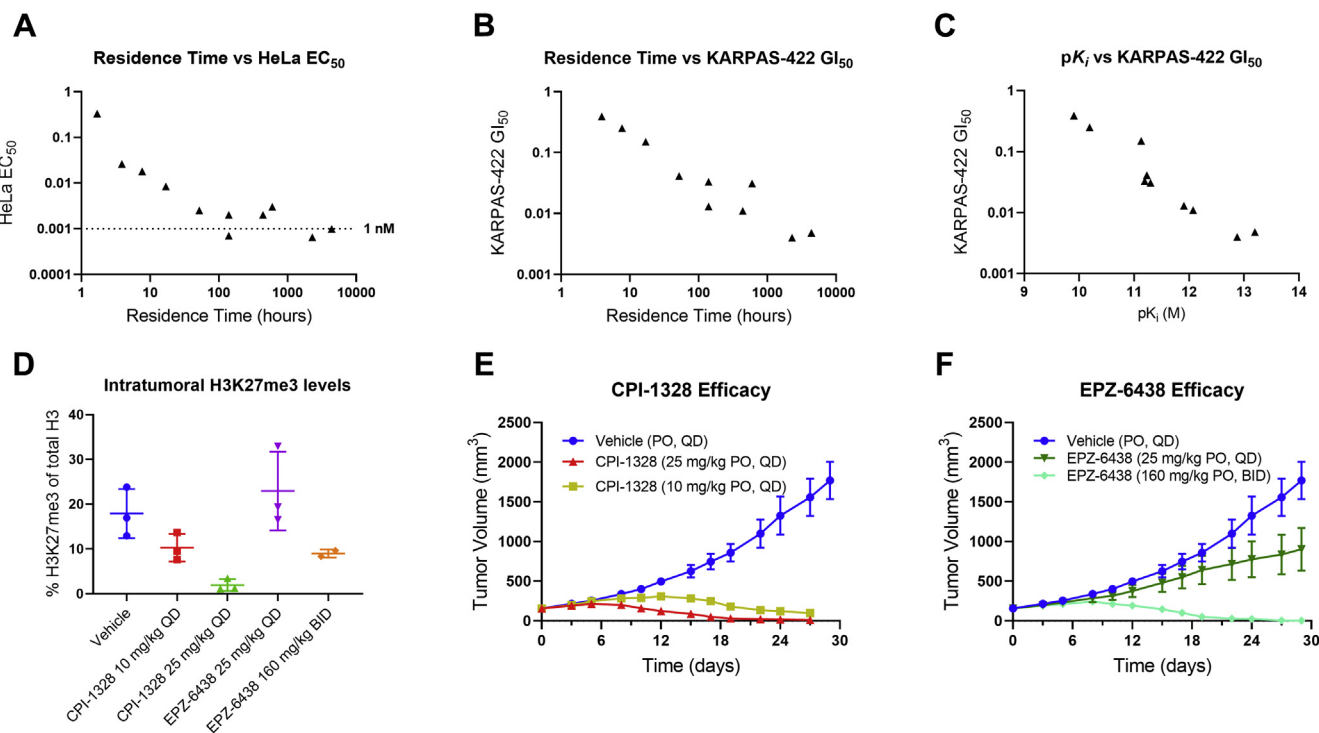


Figure 7. Biological characterization of second-generation EZH2i. A, plot of inhibitor residence time values versus EC₅₀ values for H3K27me3 reduction in HeLa cells. B, plot of inhibitor residence time values versus GI₅₀ values for KARPAS-422 cell line. C, plot of inhibitor pK_i values versus GI₅₀ values in KARPAS-422 cell line. D, modulation of global H3K27me3 levels (Day 12) in a Karpas-422 xenograft model by CPI-1328 and EPZ-6438. Data are individual replicates with error bars representing the standard deviation of the mean. E and F, efficacy of CPI-1328 and EPZ-6438 in a Karpas-422 xenograft model, respectively. Data are the average of three or more animals with error bars representing the standard error of the mean.

KARPAS-422 cells, a mutant-EZH2 lymphoma model (Fig. 7, B). In this context, there is a continuously linear correlation between residence time and GI₅₀ values that is both striking and strongly suggestive that the extremely long residence times observed in the TR-FRET assay do in fact translate into enhanced tumor cell killing in EZH2-dependent models. In addition, we find that the correlation further tightens when comparing GI₅₀ values to the overall binding affinity (Fig. 7, C).

We therefore sought to explore the impact of sub-pM binding affinities *in vivo* in the context of a KARPAS-422 xenograft model. To do this, we compared the efficacy of the first-generation EZH2i, Tazemetostat ($K_i = 64$ pM), with that of CPI-1328 ($K_i = 63$ fM). We used doses of 25 mg/kg QD and 160 mg/kg BID for Tazemetostat while using doses of 10 mg/kg and 25 mg/kg QD for CPI-1328, all given PO. The duration of treatment for CPI-1328 and Tazemetostat was 27 and 29 days, respectively. Tumor and plasma PK analysis was performed 1 h postdose on Day 12 in all samples (Fig. S12, A and B). Direct comparison of the 25 mg/kg QD arms revealed that the total concentration of Tazemetostat observed in the tumors was 730 ng/g (99.1 % PPB). For CPI-1328, the total concentration of compound present in the tumors was approximately twofold less at 350 ng/g (96.6% PPB). Total plasma levels for Tazemetostat at this time point were 6100 ng/ml. By contrast, total CPI-1328 plasma levels were significantly lower (490 ng/ml). Additionally, we obtained a more detailed plasma PK profile of CPI-1328 in both arms and observed 12 ng/ml remaining 10 h post dose (25 mg/kg QD)

and undetectable levels at 24 h, indicating a lack of accumulation *in vivo* for either arm of CPI-1328 (Fig. S12C). In spite of the significantly higher reduction in the H3K27me3 mark and tumor size by CPI-1328, no signs of overt toxicity or changes in bodyweight were observed (Fig. S12, D and E), suggesting that robust target engagement/inhibition of EZH2 is well tolerated.

We applied an MSD ELISA-based PD readout using the tumor samples collected on Day 12 to assess target engagement at each dose *via* reduction in global H3K27me3 levels. Mice treated with CPI-1328 exhibited dose-dependent reduction in H3K27me3 levels with 10 mg/kg QD CPI-1328 causing a 43% reduction in H3K27me3 levels and 25 mg/kg QD CPI-1328 causing an 89% reduction in H3K27me3 levels (Fig. 7, D). This dose-dependent reduction in intratumoral H3K27me3 levels was accompanied by a dose-dependent tumor regression profile (Fig. 7, E). Tumor regression in mice treated with 10 mg/kg QD CPI-1328 is observed at approximately Day 12 while mice treated with 25 mg/kg QD CPI-1328 experience much more rapid onset of tumor regression with decreases in tumor volume beginning at approximately Day 5. In stark contrast, no statistically significant reduction in H3K27me3 levels was observed in mice treated with Tazemetostat at 25 mg/kg QD (Fig. 7, D). Nevertheless, this dose of Tazemetostat did result in a 49% reduction in tumor volume relative to vehicle (Fig. 7, F). A similar tumor regression profile to that seen with CPI-1328 was observed with Tazemetostat with significantly higher doses given twice as frequently

(160 mg/kg BID, Fig. 7, F). This higher dose was also associated with significant loss of H3K27me3 levels, comparable with that seen in the CPI-1328, 10 mg/kg QD arm. Taken together, these data strongly support our hypothesis that more comprehensive target coverage by an EZH2i is necessary to fully realize the therapeutic benefit of targeting EZH2.

Discussion

A survey of small-molecule drugs in 2006 indicated that the median binding constant was approximately 20 nM (37). A drug or drug-like molecule with equilibrium dissociation constant for its intended target at or below 1 nM is typically regarded as a highly potent molecule (38). Therefore, it is reasonable to question the utility of superseding this potency mark. Frequently in drug discovery research, precise characterization of affinities near or below 1 nM can be challenging and is often foregone in favor of using cell-based assay formats to inform medicinal chemistry campaigns. Our data strongly argue that continued characterization of high-affinity interactions can provide novel, unique insight into SARs that may be otherwise overlooked in medicinal chemistry campaigns. Namely, although EZH2 has been the subject of a significant number of drug discovery campaigns across multiple pharmaceutical and academic organizations (7, 13–15, 17, 18, 21, 32, 39, 40), insight into the uniqueness of the 4-thiomethyl pyridone was only attained through in-depth, mechanistic studies into the kinetics of EZH2i, studies that required development and utilization of the methodologies presented here.

The affinities reported here for our most potent EZH2i rank among the highest reported for synthetic small molecules with estimates for equilibrium dissociation constants of $\sim 10^{-13}$ M (100 fM) (41). Previous analyses have indicated that the usual “limit” for noncovalent interactions appears to be $\sim 10^{-11}$ M (10 pM) (38, 41). It has been proposed that attaining potencies beyond this empirical barrier requires use of either covalent/semicovalent intermediates or transition-state analogs (38). We have been able to locate three reports of synthetic small molecules with reported sub-pM binding affinities for their intended target, all of which similarly applied kinetic methodologies to obtain their affinity estimates (42–44).

Finasteride is a mechanism-based inhibitor of 5α -Reductase that is converted by the enzyme to an NADP-dihydrofinasteride adduct. This bisubstrate analog was kinetically characterized to exhibit a K_i similar (10^{-13} M) to that seen for the most potent second-generation EZH2i described here. In the context of Finasteride, a chemical transformation occurs that results in the generation of the high-affinity intermediate, which eventually is released as a reduced form of the parent compound (42). As noted, we do not observe any evidence of a chemical transformation in the context of our second-generation EZH2i. Instead, our studies are consistent with a fully reversible, presumably noncovalent interaction with a K_i of $\sim 10^{-13}$ M.

We are aware of only two noncovalent inhibitor studies demonstrating such a high-affinity interaction. The first

Kinetic characterization of potent EZH2 inhibitors

involves high-affinity analogs of intermediates in the Spinach Ribulose 1,5-Bisphosphate Carboxylase reaction coordinate ($K_i \sim 190$ fM) (43). The second is a transition-state analog, tripeptide phosphonate inhibitor of the zinc-dependent carboxypeptidase A. Affinity estimates for this molecule were ~ 10 – 20 fM. At the time, this was speculated to be the most potent inhibition constant for a low-molecular-weight inhibitor and to our knowledge, remains such (44). Further, a cocrystal structure for this inhibitor has been solved and clearly demonstrates a noncovalent interaction anchored by the phosphonate–Zn interaction, establishing the attainability of noncovalent, femtomolar small-molecule inhibitors (45).

Significantly, our most potent second-generation EZH2i is distinct from each of these cases in that they do not show evidence of enzymatic processing nor are they analogs of a reaction intermediate. Further, they are unlikely to be transition-state analogs. The available crystallographic evidence for other pyridone-containing inhibitors indicates that these inhibitors do not bind near enough to the actual active site to function as a transition-state mimetic (16–18). In the absence of direct structural information, one of our current hypotheses for the potency enhancements bestowed by the $-SMe$ functionality is the result of the introduction of sulfur– π interactions with Phe665 and Phe686 based on the aforementioned cocrystal structures of other pyridone-based inhibitors with EZH2. This interaction has been garnering increasing interest for its role in noncovalent interactions but may certainly only be one contributing factor (46, 47).

In summary, our second-generation EZH2i is among the most potent described to date for a synthetic small molecule. Further, they represent, to our knowledge, the most potent inhibitors described, which do not rely on enzymatic processing or reaction intermediate/transition-state mimicry. Our xenograft studies clearly demonstrate that accessing such high-affinity molecules improves their ability to more comprehensively engage EZH2, thereby significantly reducing the drug burden in hypersensitive contexts. The continued depression of H3K27me3 levels by 25 mg/kg QD of CPI-1328 *versus* the same compound given 10 mg/kg QD indicates that even in this hypersensitive context, near-complete target engagement is required to access the therapeutic potential of EZH2i. We intend to further report on medicinal chemistry optimizations of thiomethyl-containing EZH2i to improve their *in vivo* utility as well as utilization of the femtomolar potencies of our inhibitors to potentially expand the clinical utility of EZH2 inhibitors.

Experimental procedures

Enzymatic assay

Inhibitor potency was assessed through incorporation of 3H-SAM into a biotinylated H3 peptide. Pentameric PRC2 composed of EZH2, EED, SUZ12, RbAp46, and RbAp48 was prepared in-house as described previously (48). (Except for SPR experiments described below, all experiments utilized pentameric PRC2.) All peptides were custom-synthesized (New England Peptide). Specifically, PRC2 (40 pM), 3H-SAM

Kinetic characterization of potent EZH2 inhibitors

(0.9 μM ; Perkin Elmer), and 2 μM H3K27me3 activating peptide (H₂N-RKQLATKAAR(Kme3)SAPATGGVKKP-amide), in a buffer consisting of 50 mM Tris (pH 8.5), 1 mM DTT, 0.07 mM Brij-35, and 0.1 mg/ml BSA, was added at 12.5 μl /well to 384-well plates (Greiner) containing 0.2 μl droplets of acoustically dispensed inhibitor in 100% DMSO (as ten-point duplicate dose–response titrations) and allowed to equilibrate at room temperature for 4–5 h. Reactions were initiated by the addition of 12.5 μl /well of 2 μM biotinylated H3K27me1 substrate peptide (H₂N-RKQLATKAAR(Kme1)SAPATGGVKKP-NTPEG Biot) in the same buffer and allowed to react at room temperature for 18–22 h. Quenching was accomplished by addition of 20 μl /well of STOP solution (50 mM Tris (pH 8.5), 200 mM EDTA, 2 mM SAH). Thirty-five microliter of the quenched solution was transferred to Streptavidin FlashPlates (Perkin Elmer), incubated 1 h, washed, and read in a TopCount plate reader (Perkin Elmer). Final DMSO concentration was 0.8% (v/v), and turnover was kept to <5%. IC₅₀ values were calculated using nonlinear least squares four-parameter fits (Genedata Screener). Due to the high potency, assays were set up under very dilute conditions (pM enzyme/inhibitor), and even with extended preincubation, full equilibration was likely not achieved.

SAM K_m determination

K_m for SAM was determined through incorporation of 3H-SAM into a biotinylated H3 peptide. Specifically, a mixture of 6 nM PRC2 and 3 μM H3K27me3 activating peptide, in a buffer consisting of 50 mM Tris (pH 8.5), 1 mM DTT, 0.07 mM Brij-35, and 0.1 mg/ml BSA, was added at 8.3 μl /well to 384-well plates (Greiner) containing a mixture of 3H-SAM and unlabeled SAM at a ratio of 1:3 in the same buffer, with twofold dilutions from 3.8 μM . Reactions were initiated by the addition of 8.3 μl /well of 3 μM H3K27me1 substrate peptide in the same buffer and allowed to react at room temperature for 1.9 h. Quenching and subsequent product detection were as described in the enzymatic assay above. As the reactions were quenched while still under steady-state conditions, final well readings were used as a proxy for initial velocity and fit to the Michaelis–Menten model in Prism 7 (GraphPad).

Enzymatic jump dilution assay

For the 100 \times jump dilution reaction, PRC2 at 20 nM was preincubated with inhibitor at a concentration 100 \times its apparent K_d for at least 2 h at room temperature in buffer (50 mM Tris(pH 8.5), 1 mM MgCl₂, 4 mM DTT, 0.07 mM Brij-35, 0.1 mg/ml BSA, 1 μM H3K27me3 activating peptide). For the 1 \times control reaction, PRC2 at 0.2 nM was preincubated with inhibitor at a concentration equal to its apparent K_d for at least 2 h at room temperature in buffer containing 1 μM 3H-SAM and 1 μM unlabeled SAM. To initiate the reactions, the 100 \times mixture was diluted 100-fold into buffer containing 5 μM biotinylated H3K27me0 substrate peptide, and buffer containing 500 μM biotinylated H3K27me0 was diluted 100-fold into the 1 \times mixture, both to a final volume of 140 μl in a 384-well polypropylene plate (Greiner). The reactions

proceeded for 10 h at room temperature. At defined time points, an 8 μl aliquot of each reaction mixture was transferred to an equal volume of STOP solution (50 mM Tris-HCl, 200 mM EDTA, 2 mM SAH, pH 8.5) in a 384-well polystyrene plate (Greiner). After the final time point, 12 μl of the quenched solutions was transferred to a streptavidin-coated FlashPlate (PerkinElmer) containing 38 μl STOP solution and allowed to incubate overnight at room temperature. The FlashPlate was then washed and read on a TopCount (PerkinElmer) plate reader. To estimate k_{off} the 100 \times jump dilution data were fit to:

$$[P] = v_s t + \frac{v_i - v_s}{k_{obs}} [1 - e^{-k_{obs} t}]$$

V_s was constrained to the slope defined by a linear fit of the 1 \times control data, and k_{obs} was corrected for rebinding using the equation in [Supplementary Note I](#).

SPR characterization

SPR method development and experiments were performed by Beactica Therapeutics (Uppsala, Sweden) on trimeric PRC2 containing EZH2, EED, and SUZ12 (BPS Biosciences). Briefly, trimeric PRC2 immobilized by amine coupling to CM7 chips (Cytiva). All experiments were performed using a BiacoreT200 instrument (Cytiva) thermostated at 25 $^{\circ}\text{C}$. The characterization of compound interactions was conducted in a 10 mM Hepes buffer at pH 7.4, with 150 mM NaCl, 2 mM DTT, 0.1% Pluronic127, 1% DMSO. For multicycle experiments, the ligands were injected in increasing concentration series for 15 s at a flow rate of 30 $\mu\text{l}/\text{min}$.

Sensorgrams were double-referenced (reference surface, blanks) prior to global analysis using a simple 1:1 binding model including a term for mass transport limitation. The dissociation constants for slow dissociating compounds were determined using the ExtRA method. The determined value for k_{off} was then locked in the global analysis of multicycle experiments. In addition, the Rmax value was fitted locally in order to compensate for a progressively blocked surface during the experiment.

TR-FRET k_{off} determination

For nondialysis k_{off} determinations, PRC2 and Eu(W1024)- α -His antibody (hereafter Eu- α -His, PerkinElmer) were combined in 70 μl assay buffer ((50 mM Hepes (pH 7.4), 100 mM NaCl, 1 mM TCEP, 0.01% Tween-20, 0.1 mg/ml BSA; f.c. 120 nM PRC2 and 120 nM Eu- α -His). The resulting 2 \times mixture was placed in an incubator for \sim 15 min at 25 $^{\circ}\text{C}$. Five microliters of the PRC2:Eu- α -His mixture was transferred to a Greiner 384-well plate. Five microliters of buffer (\pm) 2 \times compound and (\pm) activator peptide was added to respective wells containing PRC2:Eu- α -His mixture (f.c. 70 nM compound, 60 nM PRC2:Eu- α -His mixture, (\pm) 10 μM activator peptide). Mixtures were incubated for 30 min at 25 $^{\circ}\text{C}$. Five microliters of mixtures was transferred to wells containing 45 μl of 1.1 \times Biotin-EZH2i (\pm) activator and mixed thoroughly

by pipetting up and down 5–10 times. Ten microliters of diluted mixtures was diluted a second time into 90 μl of 1.1 \times Biotin-EZH2i (\pm) activator (f.c. 700 pM EZH2i, 600 pM PRC2:Eu- α -His, 760 nM Biotin EZH2i (\pm) 10 μM activator peptide). At respective time points, 18 μl of jump dilution mixtures was transferred to black ProxiPlates (PerkinElmer) prestamped with 1 μl of 19 \times SA-APC (PerkinElmer), f.c. 630 pM EZH2i, 540 pM PRC2:Eu- α -His, 684 nM Biotin EZH2i (\pm) 9 μM activator peptide, 1500 nM SA-APC). Samples were thoroughly mixed by pipetting up and down five to ten times and then read on an Envision 2104 reader (PerkinElmer) using the manufacturer's recommended filters and settings. The fractional occupancy was determined by comparison with a DMSO only (no inhibitor) and background (no PRC2) controls. Data were fit to an exponential dissociation of the form below. For experiments involving MAK-683, 10 μM (f.c) of MAK-683 was included in compound mixture as well as biotin-EZH2i mixture.

For measurements utilizing dialysis setup: PRC2 inhibitors, activator peptide, and Eu- α -His antibody were combined (V_t 117 μl) and equilibrated overnight (full complex PRC2 [f.c PRC2] 7.5 nM, activator peptide 10 μM , inhibitors 21 nM, Eu- α -His 7.5 nM). Subsequently, the mixture was combined with bio-EZH2i (total volume 175 μl ; f.c. PRC2 5 nM, activator peptide 10 μM , inhibitors 14 nM, Eu- α -His 5 nM, bio-EZH2i 1 μM), transferred to a mini-dialysis chamber (Pierce), and serially dialyzed against several 1.8 ml volumes of buffer (50 mM Hepes (pH 7.4), 100 mM NaCl, 1 mM TCEP, 0.01% Tween-20, 0.1 mg/ml BSA, 0.01% sodium azide) containing 1 μM bio-EZH2i and 10 μM activator peptide. At defined points, 4.8 μl aliquots was withdrawn from the dialysis chamber and combined with SA-APC (total volume 40 μl , f.c. PRC2 0.60 nM, activator peptide 10 μM , Eu- α -His 0.60 nM, bio-EZH2i 0.12 μM , SA-APC 1.1 μM) to create the final TR-FRET complex. Plates were incubated for 3–6 min at RT and read. The fractional occupancy was determined by comparison with a DMSO only (no inhibitor) and background (no PRC2) controls, which were subject to the same dialysis conditions. Data were fit to an exponential dissociation of the form:

$$B(t) = (B_0 - B_f)(e^{-k_{off}t}) + B_f$$

where $B(t)$ is the fraction of enzyme bound at time (t), B_0 is the fraction of enzyme bound at $t = 0$, B_f is the fraction of enzyme bound at $t = \infty$ (constrained to 0), and k_{off} is the dissociation rate constant for inhibitor with PRC2 (in units of t^{-1}).

TR-FRET k_{on} determination

The association rate constants for compounds with EZH2 were determined in an analogous fashion as the dissociation rate constant. In contrast to the dissociation rate constant determinations in which PRC2 and compound were pre-equilibrated, PRC2 and compound were combined and the fraction of bound PRC2 was sampled at different time points using bio-EZH2i to measure the final TR-FRET complex.

Kinetic characterization of potent EZH2 inhibitors

Specifically, PRC2 (which had been pre-equilibrated with Eu- α -His) and compound were combined in 50 mM Hepes (pH 7.4), 100 mM NaCl, 1 mM TCEP, 0.01% Tween-20, 0.1 mg/ml BSA, 0.01% sodium azide, and 10 μM H3K27me3 activator peptide in a total volume of 400 μl (f.c. PRC2 1.0 nM, 7.0 nM compound, Eu- α -His 1.0 nM). At defined time points, aliquots (36 μl) were withdrawn and mixed with bio-EZH2i in the same buffer to a final volume of 40 μl (f.c. PRC2 0.90 nM, compound 6.3 nM, Eu- α -His 0.90 nM, bio-EZH2i 1.2 μM). Aliquots of this mixture (36 μl) were then immediately withdrawn and mixed with SA-APC in the same buffer to a final volume of 38 μl (f.c. PRC2 0.85 nM, compound 6.0 nM, Eu- α -His 0.85 nM, bio-EZH2i 1.1 μM , SA-APC 1.5 μM). Plates were incubated for 3–6 min at RT and then read (Envision 2104), and the fractional occupancy was determined by comparison with a DMSO only (no inhibitor) and background (no bio-EZH2i) controls.

Differential scanning fluorimetry binding assays

Compound potency was assessed through differential scanning fluorimetry (DSF) in a modified TR-FRET assay buffer (50 mM Hepes (pH 7.4), 100 mM NaCl, 1 mM TCEP and 0.2% DMSO). PRC2 was combined with compounds (compounds initially in 100% DMSO) and H3K27me3 activator peptide to final concentrations of 750 nM PRC2, 20 μM compound, 200 μM activating peptide, and 4 \times PTS Dye (ThermoFisher) in a total volume of 20 μl in a MicroAmp EnduraPlate Optical 384-Well Clear Reaction Plates with Barcode (Applied Biosystems). The plate was immediately spun at 1000 RPM for \sim 30 s and sealed with a LightCycler 480 sealing foil (both Roche Diagnostics). After incubation at RT for 90 min (to allow full equilibration/binding), plates were analyzed in a Viiia7 Real-Time PCR system (ThermoFisher) in a melt curve assay where the temperature was increased from 25 $^{\circ}\text{C}$ to 95 $^{\circ}\text{C}$ at a rate of 0.05 $^{\circ}\text{C}/\text{s}$. Unliganded PRC2 complexes exhibit multiphasic melting transitions as determined by their first derivative melting curves. Melting temperatures (T_{mD}) were determined using the first derivative melting algorithm in the Protein Thermal Shift Analysis software (Applied Biosystems), and ΔT_{mD} was obtained from $T_{mD}^{\text{Cmpd}} - T_{mD}^{\text{DMSO}^{\text{ctrl}}}$. Melting temperatures were also determined using the Boltzmann method in the Protein Thermal Shift Analysis software (Applied Biosystems, [T_{mB}]).

Compound mass spectral analysis following incubation with PRC2

PRC2 was buffer exchanged into 50 mM Hepes, pH 7.4, 100 mM NaCl by dialysis (D-Tube Dialyzers, MWCO 6–8 kD, Millipore-Sigma) and concentrated to \sim 6 mg/ml (Amicon Ultra 30k, Millipore-Sigma). Titration of a potent inhibitor in the enzymatic assay showed the concentration of active enzyme to be 19 μM . Protein/Ligand incubation for MS analyses: final [conc] are PRC2 18.4 μM , 13 10 μM and \pm 30 μM H3K27me3 activator peptide with incubation for \sim 44 h at 25 $^{\circ}\text{C}$. Protein samples were denatured with an equal volume of 2% formic acid (FA) for 5 min at RT. C18 spin

Kinetic characterization of potent EZH2 inhibitors

columns (Pierce) were used to desalt protein and compound samples with resin activation with 50% acetonitrile (ACN); equilibration with 5% ACN/1% FA; wash following sample loading with 5% ACN/1% FA; elution with 70% ACN/0.1% FA. Mass spectral analysis was performed on a Synapt G2si HDMS (Waters) equipped with a nano-ESI source. The following instrument setting was used to analyze the samples: Capillary voltage was set to 1 kV, source temperature was at 30 °C, sampling cone voltage was set to 20 V, no nano gas flow was applied. MassLynx v4.2 (Waters) was used for data analysis.

H3K27me3 assessment in HeLa cells

Ten different doses of each test compound (in a series of threefold dilutions) were plated in duplicate 384-well tissue-culture-treated plates (Greiner). HeLa cells grown in culture were trypsinized and counted using a Countess cell counter (Thermo Fisher). Cells were diluted to 67,000 cells per mL in 10% DMEM (Thermo Fisher), and 15 μ l (1000 cells) was plated into each well using the Biotek MicroFlo™ Select Dispenser (BioTek Instruments, Inc) of the 384-well plate. Plates were incubated at 37 °C/5% CO₂ for 72 h. One of the duplicate plates was processed for AlphaLISA and the other for viability. (For AlphaLISA assays, all reagents were PerkinElmer and were used as provided by the manufacturer.) Five microliters per well Cell-Histone Lysis buffer (1 \times) was added to the plate processed for AlphaLISA and incubated at RT for 30 min on a plate shaker at low speed. Ten microliter per well Histone Extraction buffer was added and the plate further incubated at RT for 20 min on plate shaker with low speed. Ten microliter per well of a 5 \times mix of anti-K27me3 acceptor beads and biotinylated anti-Histone H3 (C-ter) antibody (diluted to 3 nM final concentration) was added. The acceptor beads and anti-Histone H3 were diluted in 1 \times Histone Detection buffer. The plate was sealed and incubated at RT for 1 h. Finally, 10 μ l per well of 5 \times solution of Streptavidin donor beads (20 μ g/ml final in 1 \times Histone Detection Buffer) was added, the plate sealed and incubated at RT for 30 min. The plates were read on an Envision 2104 reader (PerkinElmer) using the manufacturer's recommended filters and settings.

Cell viability was assayed by adding 15 μ l of Cell Titer Glo (Promega) to each well with cells with media. The plates were incubated at RT for 15–20 min on a plate shaker at low speed. Luminescence was read on an Envision 2104 reader (PerkinElmer) using the manufacturer's recommended filters and settings.

Data from both assays was analyzed using Genedata Screener. Readout of DMSO wells was used to normalize the data. Dose–response curves were fit using a four-parameter Hill fit with automated outlier detection and all parameters floating with a constraint on maximal effect \geq –100% activity.

KARPAS-422 GI₅₀ assay

Ten different doses of each test compound (in a series of twofold dilutions) in triplicate were plated in 96-well Corning Costar Flat Bottom Cell Culture Plates (Thermo Fisher). Cells were plated at a density of 30,000 cells/well in a total volume of

100 μ l/well. Plates were incubated at 37 °C/5% CO₂ for 96 h. Sixty microliters of fresh media was added to wells and cells were mixed by pipetting up and down \sim 15 times. Forty microliters of cell suspension was transferred to a new compound-containing 96-well plate and brought up to a final volume of 100 μ l. After 96 h (day 8), Sixty microliters of fresh media was added to wells and cells were mixed by pipetting up and down \sim 15 times. Forty microliters of cell suspension was transferred into a 96-well white plate (Corning 96-Well White Polystyrene Microplates, ThermoFisher). Equal volume of CellTiter-Glo (Promega) was added to each well. Plates were incubated at RT for 30 min with mild shaking and read as for the HeLa mark assay. Readout of DMSO wells were used to normalize the data. Dose–response data was analyzed using GraphPad Prism and a four-parameter Hill fit.

Animal use care statement

All the procedures were performed according to the guidelines approved by the Institutional Animal Care and Use Committee (IACUC) of WuXi AppTec, Shanghai, China, following the guidance of the Association for Assessment and Accreditation of Laboratory Animal Care (AAALAC).

Efficacy in KARPAS-422 xenograft model

Female CB-17 SCID mice (age 6–8 weeks) were inoculated subcutaneously (SC) at the right flank with the exponentially growing KARPAS-422 tumor cells (5×10^6) in 0.2 ml of PBS with Matrigel (1:1) at WuXi AppTech (Shanghai). The treatment was started on day 24 after tumor inoculation. Vehicle-treated mice (20% Propylene Glycol (PG) +10% Solutol HS15 + 70% 50 mM phthalate buffer (pH = 3.5), 29 days) consisted of seven randomly assigned tumor-bearing mice. Seven mice were treated with CPI-1328 25 mg/kg PO QD (27 days) while six mice respectively were treated with CPI-1328 10 mg/kg PO QD (27 days), 25 mg/kg PO QD Tazemetostat (29 days), and 160 mg/kg PO BID Tazemetostat (29 days). Mice were dosed until the tumor volume reached 2000 mm³ as per IACUC guidelines. Each group consisted of randomly assigned tumor-bearing mice. Three mice from each sample group were taken down at day 12 for PK/PD analysis. Tumor size was measured three times a week using a caliper, and the tumor volume (V) was expressed in mm³ using the formula: $V = 0.5a \times b^2$ where “a” and “b” are the long and short diameters of the tumor, respectively. The mice were weighed every day. TGI % was calculated according to the following equation: $TGI (\%) = [1 - (T_1 - T_0)/(C_1 - C_0)] \times 100$, where C₁—mean tumor volume of control mice at time t; T₁—mean tumor volume of treated mice at time t; C₀—mean tumor volume of control mice at time 0; T₀—mean tumor volume of treated mice at time 0.

Tumor pharmacodynamic assay

H3K27me3 and total H3 expression levels in tumors were analyzed by Meso Scale Discovery (MSD) ELISA. Briefly, each tumor was collected after animal euthanization, snap-frozen in liquid nitrogen, and then transferred to –80 °C before analysis. Approximately 20–30 mg of tissue was transferred in 2 ml

Eppendorf tubes. Four-hundred microliters of 1× RIPA buffer supplemented with 1× complete protease inhibitor cocktail, 1 mM PMSF, and 1:5000 Benzodase was added. Tumors were ground with a TissueLyser LT at full speed for 5 min. Samples were incubated on ice for 30 min to each sample, 100 µl of 5 M NaCl was added (1 M f.c.). Samples were mixed three to five times with a pipet and briefly vortexed. Samples were sonicated 2× for 30 s at max output power with biorupt UCD-200 (Diagenode). Samples were incubated on ice for 30 min followed by centrifugation for 10 min at 12,000g. Supernatants were transferred to a new vial, and protein concentration was determined *via* the BCA method. Lysates were diluted to a final concentration of 0.25 µg/µl using 1× RIPA buffer containing 1 M NaCl. Lysates can be stored frozen at −80 °C. MSD standard bind 96-well plates were coated with 30 µl total histone H3 capture antibody at 1 µg/ml in PBS (EMD-MAB3422). Plates were sealed and left overnight at 4 °C. Coating buffer was removed and plates were washed 3× with 150 µl of TBST. Plates were blocked with 150 µl of 5% BSA in 1× TBST at RT with shaking for 1 h. Blocking buffer was removed and plates were washed 3× with 150 µl of TBST. Lysates were diluted to a final concentration of 0.025 µg/µl per well using buffer lacking salt or detergent (sodium concentration reduced to ~100 mM). Twenty-five microliters of each sample was loaded into an individual well. Plates were incubated with lysates for 2 h at RT with shaking. Lysates were removed and plates were washed 3× with 150 µl of TBST. Twenty-five microliters of αH3K27me3 (0.25 µg/ml, Cell Signaling 9733), which had previously been validated in-house (48) or anti-Histone H3 (0.125 µg/ml, Cell Signaling 4499) in 1% BSA in TBST, was added for 30 min at RT with shaking. Twenty-five microliters per well of sulfo-tag rabbit antibody (MSD Catalog# R32AB-1) in 1% BSA in TBST (0.5 µg/ml) was added followed by incubation for 1 h at RT with shaking. Antibody mixtures were removed from wells and samples were washed 3× with 150 µl of TBST. Reading buffer (1×) was added to wells (150 µl) and plates were read on an MSD instrument.

Data availability

All data are contained within the article. For compounds that are not commercially available, detailed syntheses and characterization are found in the Supporting Information. Additionally, a comprehensive summary of biochemical data collected for each compound and presented here can be found in Tables S1 to S3.

Acknowledgments—Surface plasmon resonance studies were carried out under the direction of Per Källblad and Matthis Geitmann at Beactica AB (Uppsala, Sweden). Mass spectrometric analyses were performed on instrumentation at the UMass Amherst Mass Spectrometry Center, which is under the direction of Dr Stephen Eyles, who also provided helpful technical advice. We would also like to acknowledge our collaborators at WuXi AppTec for compound syntheses and animal studies. Lastly, we would like to thank our colleague Leslie Dakin for the synthesis of the biotinylated probe compound.

Author contributions—J. I. S., N. R. C., A. C., S. A., J. R. L., and R. T. C. conceptualization; J. I. S., N. R. C., V. V., A. R., A. K., J. B., V. S. G., and L. M. investigation; J. I. S., N. R. C., A. K., J. R. L., and J. A. M. writing- original draft; J. I. S., N. R. C., J. R. L. and R. T. C. writing-review & editing; J. R. L., R. T. C., R. J. S., J. E. A., and P. T. supervision.

Conflict of interest—The authors declare that they have no conflicts of interest with the contents of this article.

Abbreviations—The abbreviations used are: DMSO, dimethylsulfoxide; PRC2, polycomb repressive complex 2; SA-APC, streptavidin allophycocyanin; SAR, structure–activity relationship; SKR, structure–kinetic relationship; SPR, surface plasmon resonance; TR-FRET, time-resolved fluorescence energy transfer.

References

1. Strahl, B. D., and Allis, C. D. (2000) The language of covalent histone modifications. *Nature* **403**, 41–45
2. Jenuwein, T., and Allis, C. D. (2001) Translating the histone code. *Science* **293**, 1074–1080
3. Bannister, A. J., and Kouzarides, T. (2011) Regulation of chromatin by histone modifications. *Cell Res* **21**, 381–395
4. Chi, P., Allis, C. D., and Wang, G. G. (2010) Covalent histone modifications—miswritten, misinterpreted and mis-erased in human cancers. *Nat. Rev. Cancer* **10**, 457–469
5. Koschmann, C., Nunez, F. J., Mendez, F., Brosnan-Cashman, J. A., Meeker, A. K., Lowenstein, P. R., and Castro, M. G. (2017) Mutated chromatin regulatory factors as tumor drivers in cancer. *Cancer Res.* **77**, 227–233
6. Zhao, L., Duan, Y. T., Lu, P., Zhang, Z. J., Zheng, X. K., Wang, J. L., and Feng, W. S. (2018) Epigenetic targets and their inhibitors in cancer therapy. *Curr. Top. Med. Chem.* **18**, 2395–2419
7. Tanaka, M., Roberts, J. M., Qi, J., and Bradner, J. E. (2015) Inhibitors of emerging epigenetic targets for cancer therapy: A patent review (2010–2014). *Pharm. Pat. Anal.* **4**, 261–284
8. Kim, K. H., and Roberts, C. W. (2016) Targeting EZH2 in cancer. *Nat. Med.* **22**, 128–134
9. Yap, D. B., Chu, J., Berg, T., Schapira, M., Cheng, S. W., Moradian, A., Morin, R. D., Mungall, A. J., Meissner, B., Boyle, M., Marquez, V. E., Marra, M. A., Gascoyne, R. D., Humphries, R. K., Arrowsmith, C. H., *et al.* (2011) Somatic mutations at EZH2 Y641 act dominantly through a mechanism of selectively altered PRC2 catalytic activity, to increase H3K27 trimethylation. *Blood* **117**, 2451–2459
10. Majer, C. R., Jin, L., Scott, M. P., Knutson, S. K., Kuntz, K. W., Keilhack, H., Smith, J. J., Moyer, M. P., Richon, V. M., Copeland, R. A., and Wigle, T. J. (2012) A687V EZH2 is a gain-of-function mutation found in lymphoma patients. *FEBS Lett.* **586**, 3448–3451
11. McCabe, M. T., Graves, A. P., Ganji, G., Diaz, E., Halsey, W. S., Jiang, Y., Smitheman, K. N., Ott, H. M., Pappalardi, M. B., Allen, K. E., Chen, S. B., Della Pietra, A., 3rd, Dul, E., Hughes, A. M., Gilbert, S. A., *et al.* (2012) Mutation of A677 in histone methyltransferase EZH2 in human B-cell lymphoma promotes hypertrimethylation of histone H3 on lysine 27 (H3K27). *Proc. Natl. Acad. Sci. U. S. A.* **109**, 2989–2994
12. Gan, L., Yang, Y., Li, Q., Feng, Y., Liu, T., and Guo, W. (2018) Epigenetic regulation of cancer progression by EZH2: From biological insights to therapeutic potential. *Biomark Res.* **6**, 10
13. Gulati, N., Beguelin, W., and Giulino-Roth, L. (2018) Enhancer of zeste homolog 2 (EZH2) inhibitors. *Leuk. Lymphoma* **59**, 1574–1585
14. Stazi, G., Zwergel, C., Mai, A., and Valente, S. (2017) EZH2 inhibitors: A patent review (2014–2016). *Expert Opin. Ther. Pat* **27**, 797–813
15. Danishuddin, Subbarao, N., Faheem, M., and Khan, S. N. (2019) Polycomb repressive complex 2 inhibitors: Emerging epigenetic modulators. *Drug Discov. Today* **24**, 179–188

Kinetic characterization of potent EZH2 inhibitors

- Bratkowski, M., Yang, X., and Liu, X. (2018) An evolutionarily conserved structural platform for PRC2 inhibition by a class of Ezh2 inhibitors. *Sci. Rep.* **8**, 9092
- Brooun, A., Gajiwala, K. S., Deng, Y. L., Liu, W., Bolanos, B., Bingham, P., He, Y. A., Diehl, W., Grable, N., Kung, P. P., Sutton, S., Maegley, K. A., Yu, X., and Stewart, A. E. (2016) Polycomb repressive complex 2 structure with inhibitor reveals a mechanism of activation and drug resistance. *Nat. Commun.* **7**, 11384
- Vaswani, R. G., Gehling, V. S., Dakin, L. A., Cook, A. S., Nasveschuk, C. G., Duplessis, M., Iyer, P., Balasubramanian, S., Zhao, F., Good, A. C., Campbell, R., Lee, C., Cantone, N., Cummings, R. T., Normant, E., et al. (2016) Identification of (R)-N-((4-Methoxy-6-methyl-2-oxo-1,2-dihydropyridin-3-yl)methyl)-2-methyl-1-(1-(2,2,2-trifluoroethyl)piperidin-4-yl)ethyl)-1H-indole-3-carboxamide (CPI-1205), a potent and selective inhibitor of histone methyltransferase EZH2, suitable for phase I clinical trials for B-cell lymphomas. *J. Med. Chem.* **59**, 9928–9941
- Xu, C., Bian, C., Yang, W., Galka, M., Ouyang, H., Chen, C., Qiu, W., Liu, H., Jones, A. E., MacKenzie, F., Pan, P., Li, S. S., Wang, H., and Min, J. (2010) Binding of different histone marks differentially regulates the activity and specificity of polycomb repressive complex 2 (PRC2). *Proc. Natl. Acad. Sci. U. S. A.* **107**, 19266–19271
- Hansen, K. H., Bracken, A. P., Pasini, D., Dietrich, N., Gehani, S. S., Monrad, A., Rappsilber, J., Lerdrup, M., and Helin, K. (2008) A model for transmission of the H3K27me3 epigenetic mark. *Nat. Cell Biol.* **10**, 1291–1300
- Qi, W., Zhao, K., Gu, J., Huang, Y., Wang, Y., Zhang, H., Zhang, M., Zhang, J., Yu, Z., Li, L., Teng, L., Chuai, S., Zhang, C., Zhao, M., Chan, H., et al. (2017) An allosteric PRC2 inhibitor targeting the H3K27me3 binding pocket of EED. *Nat. Chem. Biol.* **13**, 381–388
- He, Y., Selvaraju, S., Curtin, M. L., Jakob, C. G., Zhu, H., Comess, K. M., Shaw, B., The, J., Lima-Fernandes, E., Szewczyk, M. M., Cheng, D., Klinge, K. L., Li, H. Q., Plushchev, M., Algire, M. A., et al. (2017) The EED protein-protein interaction inhibitor A-395 inactivates the PRC2 complex. *Nat. Chem. Biol.* **13**, 389–395
- Van Aller, G. S., Pappalardi, M. B., Ott, H. M., Diaz, E., Brandt, M., Schwartz, B. J., Miller, W. H., Dhanak, D., McCabe, M. T., Verma, S. K., Creasy, C. L., Tummino, P. J., and Kruger, R. G. (2014) Long residence time inhibition of EZH2 in activated polycomb repressive complex 2. *ACS Chem. Biol.* **9**, 622–629
- Motulsky, H. J., and Mahan, L. C. (1984) The kinetics of competitive radioligand binding predicted by the law of mass action. *Mol. Pharmacol.* **25**, 1–9
- Copeland, R. A. (2016) The drug-target residence time model: A 10-year retrospective. *Nat. Rev. Drug Discov.* **15**, 87–95
- Copeland, R. A., Pompliano, D. L., and Meek, T. D. (2006) Drug-target residence time and its implications for lead optimization. *Nat. Rev. Drug Discov.* **5**, 730–739
- Tummino, P. J., and Copeland, R. A. (2008) Residence time of receptor-ligand complexes and its effect on biological function. *Biochemistry* **47**, 5481–5492
- Quinn, J. G., Pitts, K. E., Steffek, M., and Mulvihill, M. M. (2018) Determination of affinity and residence time of potent drug-target complexes by label-free biosensing. *J. Med. Chem.* **61**, 5154–5161
- Khanna, A., Cote, A., Arora, S., Moine, L., Gehling, V. S., Brennenman, J., Cantone, N., Stuckey, J. I., Apte, S., Ramakrishnan, A., Bruderek, K., Bradley, W. D., Audia, J. E., Cummings, R. T., Sims, R. J., 3rd, et al. (2020) Design, synthesis, and pharmacological evaluation of second generation EZH2 inhibitors with long residence time. *ACS Med. Chem. Lett.* **11**, 1205–1212
- Copeland, R. A., Basavapathruni, A., Moyer, M., and Scott, M. P. (2011) Impact of enzyme concentration and residence time on apparent activity recovery in jump dilution analysis. *Anal. Biochem.* **416**, 206–210
- Yung-Chi, C., and Prusoff, W. H. (1973) Relationship between the inhibition constant (KI) and the concentration of inhibitor which causes 50 per cent inhibition (I50) of an enzymatic reaction. *Biochem. Pharmacol.* **22**, 3099–3108
- Konze, K. D., Ma, A., Li, F., Barsyte-Lovejoy, D., Parton, T., Macnevin, C. J., Liu, F., Gao, C., Huang, X. P., Kuznetsova, E., Rougie, M., Jiang, A., Pattenden, S. G., Norris, J. L., James, L. I., et al. (2013) An orally bioavailable chemical probe of the Lysine Methyltransferases EZH2 and EZH1. *ACS Chem. Biol.* **8**, 1324–1334
- McPherson, R. A., and Zettner, A. (1975) A mathematical analysis of the incubation time in competitive binding systems. *Anal. Biochem.* **64**, 501–508
- Benson, S. W. (1960) *The Foundations of Chemical Kinetics*, McGraw-Hill Book Company, New York, NY
- Boeker, E. A. (1984) Simple integrated rate equations for reversible bimolecular reactions. *Experientia* **40**, 453–456
- Gonzalez, M., Bagatolli, L. A., Echabe, I., Arrondo, J. L., Argarana, C. E., Cantor, C. R., and Fidelio, G. D. (1997) Interaction of biotin with streptavidin. Thermostability and conformational changes upon binding. *J. Biol. Chem.* **272**, 11288–11294
- Overington, J. P., Al-Lazikani, B., and Hopkins, A. L. (2006) How many drug targets are there? *Nat. Rev. Drug Discov.* **5**, 993–996
- Smith, A. J., Zhang, X., Leach, A. G., and Houk, K. N. (2009) Beyond picomolar affinities: Quantitative aspects of noncovalent and covalent binding of drugs to proteins. *J. Med. Chem.* **52**, 225–233
- Kung, P. P., Bingham, P., Brooun, A., Collins, M., Deng, Y. L., Dinh, D., Fan, C., Gajiwala, K. S., Grantner, R., Gukasyan, H. J., Hu, W., Huang, B., Kania, R., Kephart, S. E., Krivacic, C., et al. (2018) Optimization of orally bioavailable enhancer of zeste homology 2 (EZH2) inhibitors using ligand and property-based design strategies: Identification of development candidate (R)-5,8-Dichloro-7-(methoxy(oxetan-3-yl)methyl)-2-((4-methoxy-6-methyl-2-oxo-1,2-dihydropyridin-3-yl)methyl)-3,4-dihydroisoquinolin-1(2H)-one (PF-06821497). *J. Med. Chem.* **61**, 650–665
- Honma, D., Kanno, O., Watanabe, J., Kinoshita, J., Hirasawa, M., Nosaka, E., Shiroishi, M., Takizawa, T., Yasumatsu, I., Horiuchi, T., Nakao, A., Suzuki, K., Yamasaki, T., Nakajima, K., Hayakawa, M., et al. (2017) Novel orally bioavailable EZH1/2 dual inhibitors with greater antitumor efficacy than an EZH2 selective inhibitor. *Cancer Sci.* **108**, 2069–2078
- Kuntz, I. D., Chen, K., Sharp, K. A., and Kollman, P. A. (1999) The maximal affinity of ligands. *Proc. Natl. Acad. Sci. U. S. A.* **96**, 9997–10002
- Bull, H. G., Garcia-Calvo, M., Andersson, S., Baginsky, W. F., Chan, H. K., Ellsworth, D. E., Miller, R. R., Stearns, R. A., Bakshi, R. K., Rasmusson, G. H., Tolman, R. L., Myers, R. W., Kozarich, J. W., and Harris, G. S. (1996) Mechanism-based inhibition of human steroid 5 α -reductase by finasteride: Enzyme-catalyzed formation of NADP-dihydrofinasteride, a potent bisubstrate analog inhibitor. *J. Am. Chem. Soc.* **118**, 2359–2365
- Schloss, J. V. (1988) Comparative affinities of the epimeric reaction-intermediate analogs 2- and 4-carboxy-D-arabinitol 1,5-bisphosphate for spinach ribulose 1,5-bisphosphate carboxylase. *J. Biol. Chem.* **263**, 4145–4150
- Kaplan, A. P., and Bartlett, P. A. (1991) Synthesis and evaluation of an inhibitor of carboxypeptidase A with a Ki value in the femtomolar range. *Biochemistry* **30**, 8165–8170
- Kim, H., and Lipscomb, W. N. (1991) Comparison of the structures of three carboxypeptidase A-phosphonate complexes determined by X-ray crystallography. *Biochemistry* **30**, 8171–8180
- Beno, B. R., Yeung, K. S., Bartberger, M. D., Pennington, L. D., and Meanwell, N. A. (2015) A survey of the role of noncovalent sulfur interactions in drug design. *J. Med. Chem.* **58**, 4383–4438
- Valley, C. C., Cembran, A., Perlmutter, J. D., Lewis, A. K., Labello, N. P., Gao, J., and Sachs, J. N. (2012) The methionine-aromatic motif plays a unique role in stabilizing protein structure. *J. Biol. Chem.* **287**, 34979–34991
- Garapaty-Rao, S., Nasveschuk, C., Gagnon, A., Chan, E. Y., Sandy, P., Busby, J., Balasubramanian, S., Campbell, R., Zhao, F., Bergeron, L., Audia, J. E., Albrecht, B. K., Harmange, J.-C., Cummings, R., and Trojer, P. (2013) Identification of EZH2 and EZH1 small molecule inhibitors with selective impact on diffuse large B cell lymphoma cell growth. *Chem. Biol.* **20**, 1329–1339